Selective Grafting of Phosphorus onto $Ti_3C_2T_x$ MXene Enables Two-Proton Process and Enhanced Charge Storage

Hao Li[1,7], Ke Fan[1,7], Pei Xiong[1], Hanmo Zhou[1], Zezhou Lin[1], Keyu Tao[2], Tiancheng Liu[1], Xuyun Guo[1], Ye Zhu[1], Lyuchao Zhuang[1], Wei Han[3], Chen Yang[1], Yan Liu[4], Molly Meng-Jung Li[1*], Mingwang Fu[5], John Wang[6], Haitao Huang[1]*

[1]Department of Applied Physics and Research Institute for Smart Energy
The Hong Kong Polytechnic University
Hung Hom, Kowloon, Hong Kong 999077, P. R. China
E-mail: molly.li@polyu.edu.hk (Molly Meng-Jung Li)
aphhuang@polyu.edu.hk (Haitao Huang)

[2]College of Chemistry and Chemical Engineering,
Chongqing University
Shapingba, Chongqing 401331, P. R. China

[3]Hubei Yangtze Memory Laboratories
Wuhan, Hubei, 430205, P. R. China

[4]School of Chemical Engineering and Technology,
Sun Yat-sen University
Tangjiawan, Zhuhai 519082, P. R. China

[5]Department of Mechanical Engineering,
The Hong Kong Polytechnic University
Hung Hom, Kowloon, Hong Kong 999077, P. R. China

[6]Department of Materials Science and Engineering
National University of Singapore
117574, Singapore

[7] These authors contributed equally to this work

Abstract

$Ti_3C_2T_x$ MXene shows great promise as a supercapacitor electrode material owing to its high conductivity and pseudocapacitive nature. Phosphorus doping is an efficient strategy to boost its capacitance due to synergistic effect of the P-O and P-C species formed. However, the contribution to enhanced capacitance from specific phosphorus doped species in P-doped $Ti_3C_2T_x$ remains largely unexplored. Herein, phosphorus atoms are selectively grafted onto $Ti_3C_2T_x$ MXene, introducing only P-O doped species and how this doping configuration contributes to capacitance is unraveled. The results show that 2.1 at. % P-doped $Ti_3C_2T_x$ delivers a capacitance enhancement of 35% (437 F g^{-1} at 2 mV s^{-1}) in comparison with pristine MXene and outstanding cyclic stability. Multiple *in situ* and *ex situ* characterizations along with DFT calculations collectively reveal that the formed P-O bonds are new active sites for a two-proton bonding-debonding process, leading to the enhanced charge storage and capacitive performance in MXene. However, higher surface phosphorus doping would destroy crystal integrity of MXene and leads to performance deterioration.

Key words: $Ti_3C_2T_x$ MXene, phosphorus doping, supercapacitors, supercapacitive mechanism.

1. Introduction

Two-dimensional (2D) materials, such as graphene, transition metal chalcogenides (TMDs) and MXenes are promising electrode materials for high power electrochemical energy storage devices (including batteries and supercapacitors) due to the merits of high specific area, low ion diffusion barrier and short ion transport path.[1-3] Their electrochemical performance can be further boosted by heteroatom incorporation that adjusts crystal structure and electron states of materials.[2, 4] Doping elements, amount and sites synergistically determine the performance change of the doped materials. For instance, surface O doping can endow graphene with extra pseudocapacitance but decreased charge mobility, while incorporation of nitrogen into the lattice of graphene not only offers new active sites for pseudocapactive reactions but also improves its charge carrier concentration.[5, 6] MXenes has been investigated as pseudocapacitive electrode materials since they were discovered in 2011, owing to their metallic conductivity (up to 2.4×10^6 S/m), hydrophilic surface, and outstanding capacitance as well as cycling stability in acidic electrolyte.[1, 7-10] But the heteroatom doping to boost charge storage in MXenes is more complicated than graphene and TMDs due to their special chemical composition and crystal structure.[11]

MXenes have a general formula of $M_nX_{n+1}T_x$, where M represents early transition metal (Ti, Cr, V, Mo, Nb, Zr, Hf, Ta, Sc, W, and Y), X is C and/or N, and T refers to functional groups linked with surface metal atoms of the material, e.g., -O, -OH, -F, and -Cl.[12, 13] A typical synthesis method of MXenes is selectively etching off A-layer of hexagonal stratified $M_{n+1}AX_n$ (MAX) precursors in hydrofluoric acid or other etchant.[12, 14, 15] When heteroatoms are incorporated into MXenes, M, X, and T are three kinds of available doping sites. Therefore, the doping of different element may give rise to different doping configurations that contribute differently to performance variation of MXenes. $Ti_3C_2T_x$ is the most studied MXene for supercapacitor electrode material and delivers the highest specific capacitance in acidic electrolyte among all as-made MXenes, which store energy via proton bonding/debonding with surface oxygen terminals.[16, 17] Phosphorus has been doped into $Ti_3C_2T_x$, MXene to boost its supercapacitive performance.[18-20] The doped atoms either fill surface titanium vacancies to form P-C bonds or are grafted onto the surface oxygen terminations with the formation of P-O species.[18-21] Ti-P bonds through substituting T sites within $Ti_3C_2T_x$ are rarely reported due to high formation energy.[18] Note that P-C bonds and P-O bonds simultaneously exist in P-doped MXene in previous studies and the ameliorative capacitance is largely attributed to a "synergistic effect" of P-C and P-O species,[18-21] while the underlying mechanism that how each specific phosphorus doping configuration cannot be differentiated. Especially, P-O bonds are the outmost functional groups on MXene surface, which directly influence the interaction between MXene and electrolyte ions. Therefore, its role in boosting capacitance needs to be critically evaluated.

Herein, phosphorus atoms are selectively grafted onto $Ti_3C_2T_x$ surface though oxygen bridging by heating the MXene aerogel in mixed atmosphere of argon and phosphine that is decomposed from sodium hypophosphite (Figure 1a), leading to the solely formation of P-O doped species. The underlying mechanism of how the P-O bonds boost charge storage capability of MXene is unraveled by combining X-ray diffraction (XRD), X-ray absorption near edge structure spectra (XANES), X-ray photoelectron spectroscopy (XPS), and in situ Raman spectroscopy. The results shows that the selectively phosphorus-doped $Ti_3C_2T_x$ MXene (PMX) with 2.1 wt% P shows a high gravimetric capacitance of 437 F g^{-1} at 2 mV s^{-1} in 1M H_2SO_4 electrolyte, much superior to that of pristine MXene (324 F g^{-1}). The formed surface P-O (Ti-O-P) groups act as new active sites for more proton bonding/debonding and thereby result in greater valence state variation of titanium during charge/discharge process (Figure 1b-d). It is also revealed that the moderate surface phosphorus doping can maintain the MXene crystal structure intact and boost the capacitance, but further incorporation of the hybrid element would injure the crystal structure and even induce amorphization, adverse to its energy storage ability.

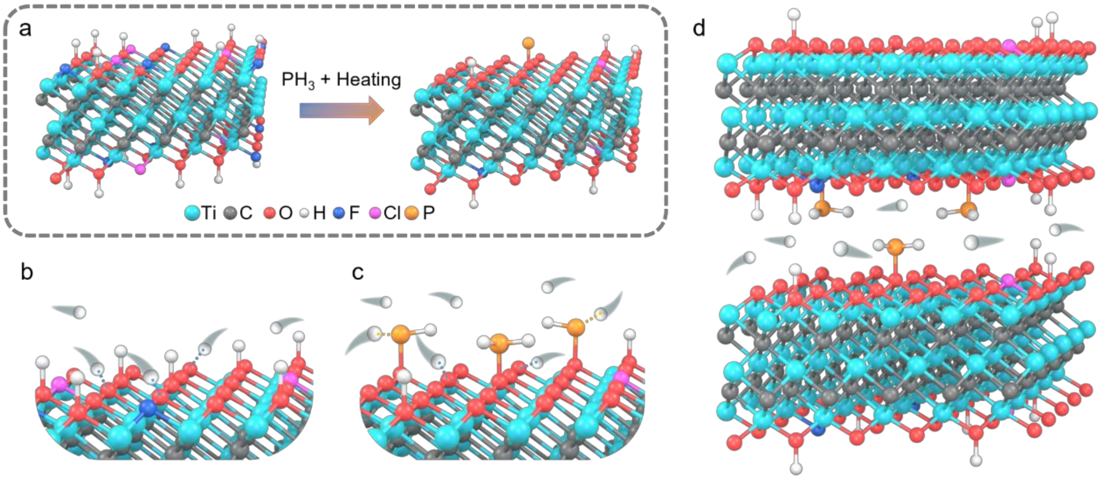

Figure 1 Schematic illustration for (a) phosphorus doping strategy, (b) proton interaction with surface of pristine $Ti_3C_2T_x$, and (c)-(d) proton interaction with surface of PMX.

2. Results and discussion

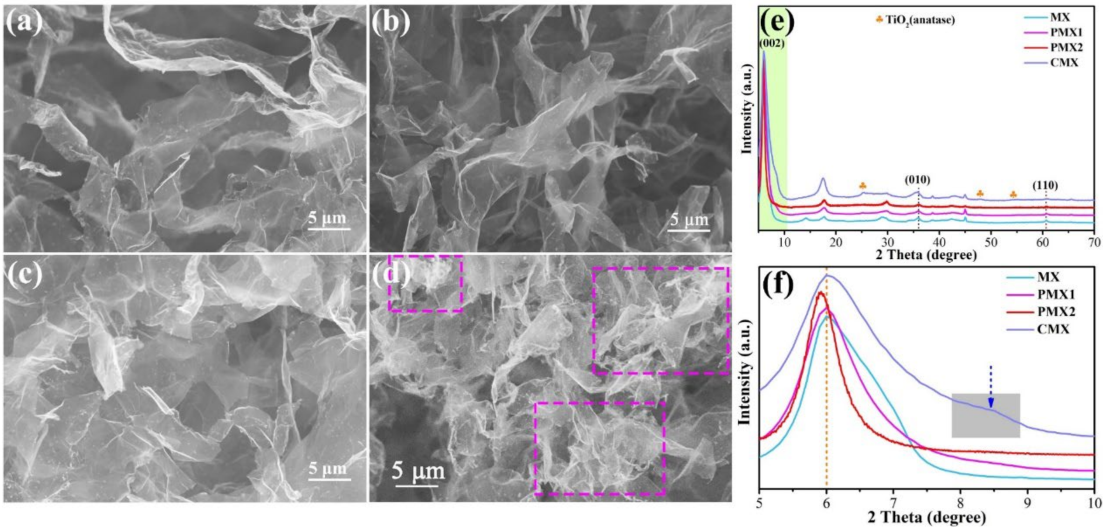

Figure 2 SEM images of (a) MX, (b) PMX1, (c) PMX2 and (d) CMX. (e) XRD patterns of the samples. (f) Enlarged (002) peak in (e).

Multilayered $Ti_3C_2T_x$ MXene was first prepared by selectively etching the aluminum layer of Ti_3AlC_2 precursor in HCl and LiF mixed liquid, followed by fierce oscillation for its delamination to obtain few-layered MXene. The resultant MXene aqueous solution shows Tyndall effect when a ray transmits through it (Figure S1a), indicating its colloidal nature. The diameter of MXene sheets is 0.50~8 µm, as confirmed by the scanning electron microscope (SEM) image (Figure S1b). The atomic force microscope (AFM) result shows that the MXene sheets have a thickness of 5.56 nm (Figure S1c), corresponding to a stacking of 5-6 layers. P-C doped species forms at titanium vacancies, and the long-time heating aggravates the formation of the vacancies and the doped species.[19] Thus, selective doping with only P-O doped bonds requires $Ti_3C_2T_x$ MXene with little defects and short doping time. The defects of $Ti_3C_2T_x$ are suppressed by etching Ti_3AlC_2 precursor with argon bubbling in this work.[10] Gas-state doping strategy (Figure 1a) was applied here to avoid the subsequent cumbersome washing procedures for removing residual doping source. To increase doping efficiency and shorten doping time, the MXene sheets were assembled into porous MXene aerogel (Figure 2a and Figure S1d) by flash freezing the MXene solution and subsequent freeze-drying.[22] Sodium hypophosphite was heated at 350°C to produce phosphine, which was brought by flowing Ar to the downstream MXene aerogel (at 400°C) to fulfill the phosphorus doping within 2 hours. The mass ratio between MXene and NaH_2PO_2 was varied from 1:1 to 1:2 to tune phosphorus doing amount, and the obtained samples were named as PMX1 and PMX2, respectively. Meanwhile, a control sample (CMX) was also fabricated by heating pristine $Ti_3C_2T_x$ MXene aerogel (MX) in pure argon under the same heating conditions as those used in the doping process.

SEM results show that both PMX1 and PMX2 retain a similar macroporous structure to that of MX (Figure 2b-c) after phosphorous incorporation, implying the robust pore structure in the MXene aerogel. Alike porous structure is also observed in CMX, but with some white spots (enclosed by the pink rectangles in Figure 2d), which could be due to the oxidation of $Ti_3C_2T_x$. The existence of titanium dioxide in CMX is confirmed from the XRD results, while no distinct oxide peaks are detected in both PMX1 and PMX2, as shown in Fig.2e. This result implies that phosphine not only serves as doping source but also restricts the thermal degradation of $Ti_3C_2T_x$. The position and full width at half maximum (FWHM) of the (002) XRD peak of MXene can reveal the changes of interlayer distance (d) and crystallinity, respectively, in $Ti_3C_2T_x$ MXene.[23] Enlarged (002) peaks of the samples are shown in Figure 2f. MX shows an unsymmetrical (002) peak at 2θ value of 6.02° and a right shoulder, indicating its main interlayer space of 14.67 Å and smaller interlayer distance for some of the MXene sheets. The (002) peak of PMX1 keeps at 6.02° but its FWHM becomes narrower than MX, which implies increased uniformity of interlayer distance. Noticeably, the (002) peak of PMX2 left shifts to 5.91° (d=14.94 Å) with smaller FWHM than MX, manifesting its more spacious and uniform interlayer path of MXene sheets due to phosphorus doping. This broadened but uniform interlayer path is expected to boost ion diffusion to active sites.[24] However, CMX without phosphorus doping shows a much broader (002) peak than the other samples, implying the inferior MXene crystallinity and non-uniform interlayer path. The peak shoulder at $2\theta \approx 8.52°$ in CMX is indicative of the presence of some MXene sheets with narrower interlayer path, which could originate from interlayer shrinkage of MXene during its heating process.[25] Overall, XRD results demonstrate that the phosphorus incorporation not only boosts the interlayer space of MXene but also retards its oxidation during heating process.

Nitrogen gas adsorption/desorption at 77K was conducted to analyze specific surface area and pore size distribution of the samples (Figure S2a-b). The Brunauer−Emmett−Teller (BET) surface area of MX is 41.03 m^3 g^{-1}, while those of PMX1, PMX2 and CMX are increased to 43.88, 41.83 and 47.63 m^3 g^{-1}, respectively (Figure S2a). These results indicate that the heating procedure (400℃) causes the enhancement of specific surface area of MXene aerogel, while P-doped MXene (PMX1, PMX2) exhibits a lower increment than that with only heating (CMX). The less increment of specific surface area in P-doped MXene can be attributed to their suppressed oxidation, while the larger increment of specific surface area in CMX could be due to its oxidation induced breakage of MXene sheets. Figure S2b indicates that MX, PMX1, PMX2 and CMX all possess a similar hierarchical pore size distribution (1.50~150 nm). But P-doped samples, especially PMX2, exhibit a higher differential pore volume at pore width of ~1.50 nm (inset of Figure S2b), probably resulting from the phosphorus incorporation.

To further investigate the crystal structure change of MX after phosphorus doping, High resolution transmission electron microscope (HRTEM) and selected area electron diffraction (SAED) characterizations were carried out (Figure 3). HRTEM images show that the phosphorus doping in PMX1 and PMX2 has not led to obvious variation of interplanar distance of (010) planes in $Ti_3C_2T_x$ MXene (Figure 3a-c), which is consistent with the XRD results of MX, PMX1 and PMX2 showing almost identical (010) peak locations (Figure 2e). However, CMX possesses a larger (010) interplanar distance (0.26 nm), consistent with its left shifted (010) diffraction peak compared with MX (Figure 2e). The SAED pattern (Figure 3a) of MX demonstrates the hexagonal symmetry of $Ti_3C_2T_x$ MXene inherited from Ti_3AlC_2 parent phase.[7] Its innermost circle of diffraction points corresponds to (010) planes and the second circle of diffraction points originates from (110) planes.[26] PMX1 and PMX2 with different doping contents exhibit the identical crystal symmetry with pristine MX, as shown in Figure 3b-c. However, if the doping amount is further enhanced via increasing the mass ratio of NaH_2PO_2 : MXene to 8 and 20 (with corresponding samples named as PMX8 and PMX20, respectively), shortened interplanar distance of (010) planes is observed in PMX8 (Figure S3a-b), and amorphization is observed in PMX20 (Figure S3c-d), accompanied by the disappearance of the six-fold symmetry of (010) planes (Figure S3e). These results conclude that large doping amount of phosphorus would break the crystal periodicity and symmetry of $Ti_3C_2T_x$ MXene. By contrast, CMX exhibits diffraction rings showing its polycrystalline nature, and some newborn diffraction points corresponding to TiO_2 anatase phase (Figure 3d), collectively verifying the fragmentation and oxidation of MXene sheets in the sample, which is also consistent with the foregoing XRD and BET results.

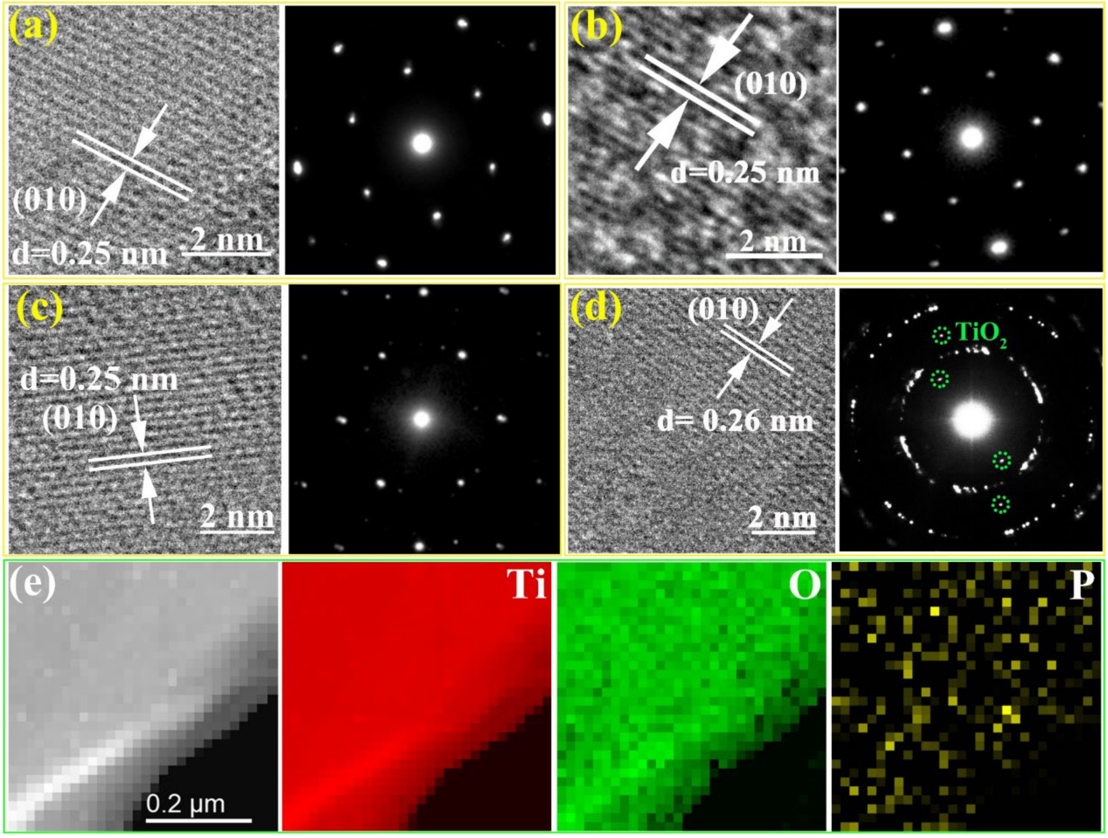

Figure 3 HRTEM images and corresponding SAED patterns of (a) MX, (b) PMX1, (c)

PMX2 and (d) CMX, respectively. (e) EELS elemental mapping results (Ti, O, P) of PMX2.

Electron energy loss spectroscopy (EELS) was conducted to analyze the elemental distribution and change of chemical environment with phosphorus incorporation in P-doped MXene. For simplicity, only MX, PMX2 and CMX are selected for EELS analysis. Both O K-edge and Ti $L_{2,3}$-edge spectra of the samples were normalized to their corresponding Ti L_2 peak intensities, as shown in Figure S4a-b. PMX2 exhibits the highest O K-edge intensity after the normalization (Figure S4b), implying its richest oxygen composition. It also denotes that the doped phosphorus could be favorable for maintaining more surface oxygen on $Ti_3C_2T_x$. In addition, asymmetric O K-edge is detected in CMX, which can be attributed to the titanium dioxide (anatase) formed in the sample.[27] Note that the first peak in O K-edge spectra is ascribed to the hybridization between Ti 3*d* orbitals and surface oxygen terminations.[28] To compare the chemical environment of oxygen in the samples, their O K-edge EELS spectra are normalized to the first peak (Figure S4c). The almost identical shape of the first O-K edge peaks for MX and PMX2 indicate that the oxygen maintains bonding with the titanium after the phosphorus incorporation. But the difference in peak 2 of O K-edge spectra between pristine MX and PMX2 confirms the change of local environment of oxygen atoms in PMX2,[27] which could be attributed to the introduced hybrid phosphorus element. The detailed change on chemical valence and environment will be discussed in the following XPS and extended X-ray absorption fine structure (EXAFS) results. The EELS element mapping of PMX2 (Figure 2e) shows the doped phosphorus is uniformly dispersed at a nanometer scale, and energy-dispersive X-ray spectroscopy (EDS) elemental mapping results (Figure S5) also demonstrate a uniform distribution of phosphorus over a larger area.

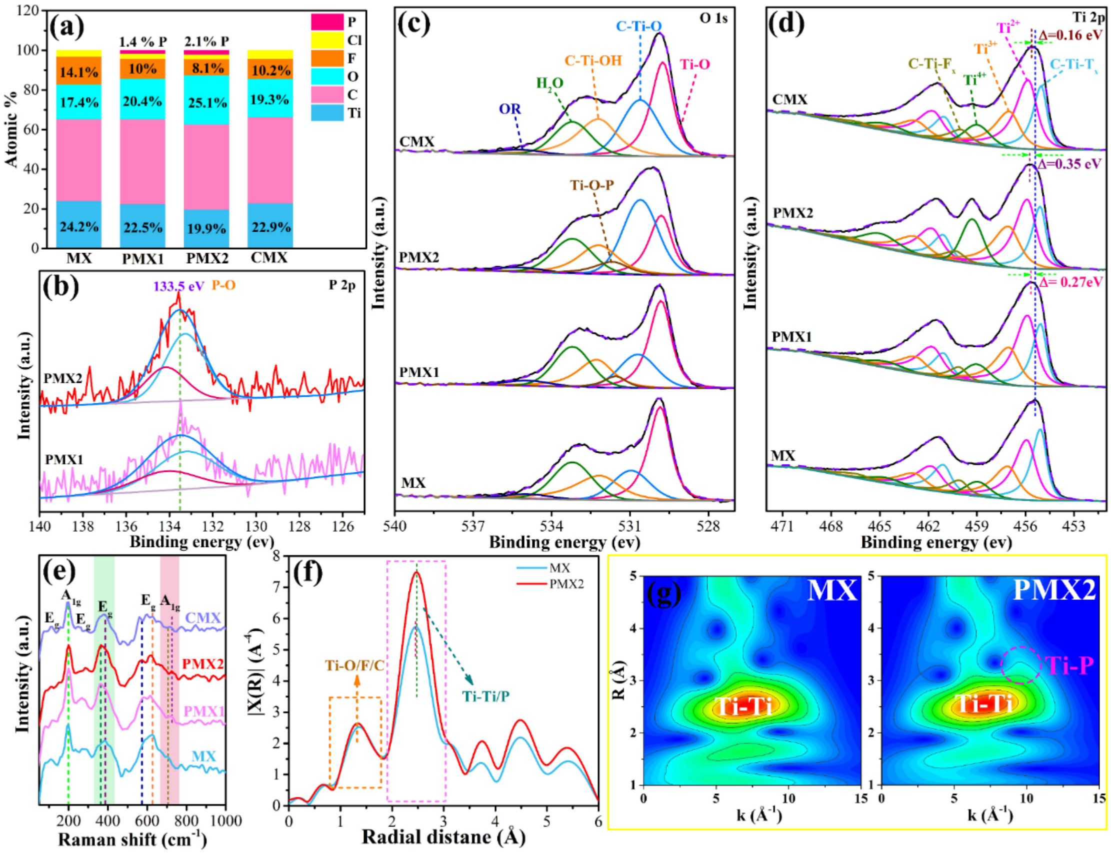

Figure 4 (a) Composition analysis of MX, PMX1, PMX2 and CMX from XPS survey spectra. (b) High resolution P2p XPS spectra of PMX1 and PMX2. High resolution (c) O1s and (d) Ti2p XPS spectra of MX, PMX1, PMX2 and CMX. (e) Raman spectrum of the samples. (f) Ti K-edge of EXAFS spectra and (g) WT-EXAFS profiles for MX and PMX2

The composition of samples was investigated by XPS survey spectra and shown in Figure 4a. PMX1 and PMX2 possess 1.4 and 2.1 at.% phosphorus, respectively, implying the successful phosphorus incorporation and the doping amount increases with increasing amount of NaH_2PO_2 added. It is also noted that PMX1 and PMX2 have 20.4 and 25.1 at.% oxygen contents, respectively, which are higher than those of MX and CMX (17.4 and 19.3 at.%, respectively). This indicates that the doped phosphorus is favorable for keeping surface oxygen on $Ti_3C_2T_x$, consistent with aforementioned EELS results (Figure S4b). In the meantime, the less contents of -F and -Cl in PMX2 than those in MX and CMX indicate that halogen terminations may be more easily eliminated in reducing atmosphere (PH_3). All XPS spectra were calibrated through C-Ti-T_x bond (282 eV) in C 1s for reliable analysis,[29] as shown in Figure S6. P 2p high resolution XPS spectra (Figure 4b) demonstrate that the formed P species contains P-O bond in both PMX1 and PMX2, corresponding to the binding energy of 133.5 eV.[30] Because of the absence of Ti-P bond (129 eV) in P 2*p*,[30] the doped phosphorus is only grafted onto $Ti_3C_2T_x$ MXene via surface oxygen bridging, forming Ti-O-P bond. This result demonstrates that the applied doping strategy successfully achieves the selective phosphorus doping with the only formation of P-O doped species. Density functional theory (DFT) calculation results (Figure S7) further verify that Ti-O-P bond can stably exist on $Ti_3C_2T_x$ surface. And it is predicted that the adjacent phosphorus atoms grafted on the surface tend to interact each other and bond together (Figure S8), which could adversely affect the crystal structure of MXene due to lattice stress. This calculation result also explains why high surface P-doping damages the crystallinity of MXene and even leads to its amorphization, as observed in PMX8 and PMX20. O 1s of MX and CMX (Figure 4c) can be deconvoluted into Ti-O, C-Ti-O, C-Ti-OH, H_2O and organics (OR), which correspond to binding energies of 529.8, 531, 532.2, 533.2, and 534.9 eV, respectively.[29, 31] However, for PMX1 and PMX2, some of their surface C-Ti-O was grafted with phosphorus, leading to the formation of Ti-O-P bond at a higher binding energy (531.6 eV)[32], and the amount of Ti-O-P increases with increasing phosphorus doping amount, as shown in the middle two spectra of Figure 4c. The comparison of Ti 2*p* of different samples is shown in Figure 4d. The binding energies for Ti 2p3 peak of PMX1 and PMX2, and CMX exhibit blue shifts of 0.27, 0.35, and 0.16 eV, respectively, compared with that of MX, indicating their elevated titanium valence states, which is similar to the case of nitrogen doped $Ti_3C_2T_x$ MXene.[23]. Titanium with higher valence states due to the phosphorous doping in PMX1 and PMX2 are expected to contribute more charge transfer during charge/discharge process.[23, 33]

Surface sensitive Raman spectra of MX, PMX1, PMX2 and CMX are shown in Figure 4e. The E_g band at 230~470 cm^{-1} represents the in-plane vibration of surface functional groups linked with outer titanium atoms in $Ti_3C_2T_x$ and the A_{1g} band at around 720 cm^{-1} is attributed to out-of-plane vibrations of carbon.[34] The wavenumbers of the E_g band in PMX1 and PMX2 are similar (370 cm^{-1}) but less than those (~ 382 cm^{-1}) of MX and CMX, suggesting that the incorporation of phosphorus engenders attenuated bond strength between functional groups and surface titanium atoms in MXene. And a larger wavenumber of the A_{1g} band (~720 cm^{-1}) is observed in P-doped $Ti_3C_2T_x$, which indicates the enhanced Ti-C bond strength after P-doping. The change of the A_{1g} band with applied potential can be used to investigate the charge storage behavior of $Ti_3C_2T_x$,[34] which will be discussed in the following sections for differentiating the energy storage behavior in P-doped $Ti_3C_2T_x$ MXene from that in pristine MXene.

The effect of incorporated P on coordination environment of Ti in $Ti_3C_2T_x$ is investigated via EXAFS. Figure 4f compares the Fourier-transform (FT) Ti K-edge EXAFS results of MX and PMX2. FT-EXAFS of both samples display two peaks in the range of 1.0−2.0 Å and 2.0−3.0 Å, corresponding to the Ti-O/F/C and Ti-Ti contribution, respectively.[35] However, PMX2 exhibits a much higher 2nd-shell peak than MX, which is assigned to an extra Ti-P coordination at 3.48 Å in PMX according to EXAFS fitting results (Fig S9 and Table S1) and DFT models (Figure S7b). The EXAFS Ti K-edge wavelet transform (WT) results (Figure 4g) consistently show that PMX2 exhibits increased intensity at both larger K and R space of Ti-Ti coordination compared to MX, as circled by pink line, which corresponds to Ti-P coordination. Therefore, these results collectively further confirm Ti-O-P coordination in P-doped MXene.

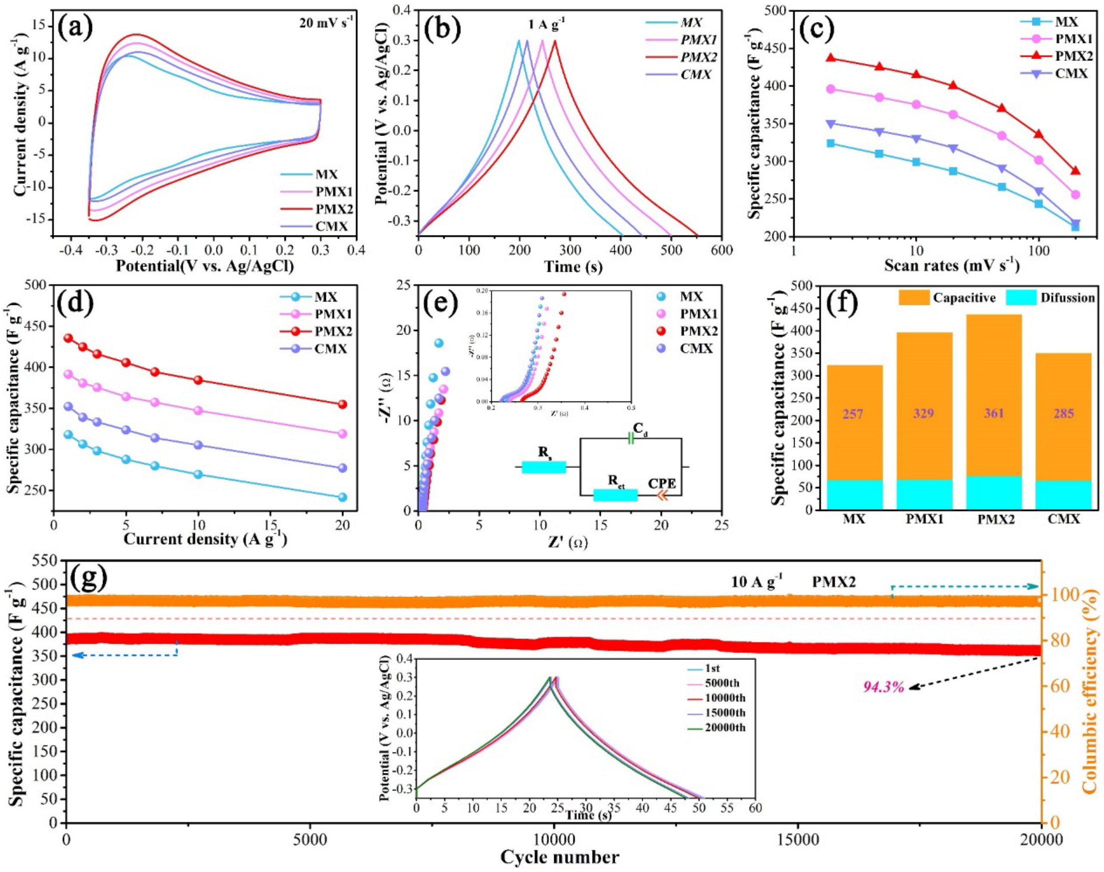

Figure 5 (a) CV curves of MX, PMX1, PMX2 and CMX at the scan rate of 20 mV s^{-1} and (b) GCD curves at the current density of 1 A g^{-1} for the four samples. Specific capacitances of the samples at (c) scan rates from 2 to 200 mVs^{-1} and (d) current densities of 1 - 20 A g^{-1}. (e) EIS spectra for the samples at -0.20 V vs. Ag/AgCl. Insets are the enlarged EIS spectra at intercept with real axis and the fitted equivalent circuit. (f) Capacitive contributions of the four samples at 2 mV s^{-1}. (g) Cyclic test of PMX2 at 10 A g^{-1}. Inset shows its GCD curves at different cycles.

The electrochemical performances (ECs) of the as-prepared samples were studied in 1M H_2SO_4 with three-electrode configuration, in which Ag/AgCl (sat. KCl) and graphite bar are reference and counter electrodes, respectively. Figure 5a shows cyclic voltammetry (CV) profiles of MX, PMX1, PMX2 and CMX at a scan rate of 20 mV s^{-1}. Redox peaks are observed in all of them, implying their pseudocapacitive energy storage mechanism.[33, 36] PMX1 and PMX2 exhibit larger integral areas than MX and CMX, indicative of their higher capacitances. In addition, PMX2 with richer phosphorus doping exhibits better energy storage ability than PMX1. A similar result is also shown in galvanostatic charge/discharge (GCD) curves (Figure 5b). These enhanced capacitances in PMX1 and PMX2 should be attributable to the incorporated phosphorus. The capacitances of the samples at various scan rates (2-200 mV s^{-1}) and current densities (1 - 20 A g^{-1}) are compared and summarized in Figure 5 c-d. PMX2 delivers the highest capacitances of 437 F g^{-1} and 435 F g^{-1} at 2 mV s^{-1} and 1 A g^{-1}

respectively, which are comparable with and even higher than those of other heteroatom doped (N, S, V etc.) $Ti_3C_2T_x$ MXene, as demonstrated in Table S2. To investigate the effect of phosphorus doping amount on ECs, PMX8 (2.8 at. % P) and PMX20 (3.5 at. % P) were also studied, and the corresponding results are shown in Figure S10. Unfortunately, further increase in phosphorus doping does not contribute to better energy storage ability but result in performance deterioration, which could be attributed to their degraded crystallinity (Figure S3).

Electrochemical impedance spectroscopy (EIS) results were used to evaluate redox kinetics and electrical conductivity of different samples. The Nyquist plots of MX PMX1, PMX2 and CMX at -0.20 V vs. Ag/AgCl are shown in Figure 5e. The slope of linear part of the plots reflects ion diffusion resistance in electrode materials. The similar slope of the four samples implies that the surface grafted phosphorus atoms on $Ti_3C_2T_x$ do not block electrolyte ions to active sites. The semicircle of the Nyquist plot (upper inset of Figure 5e) at high frequency range denotes the charge transfer resistance (R_{ct}) at electrode/electrolyte interface.[37] Its intercept with real axis in the plot represents equivalent series resistance (R_s), which is composed of electrical resistance of electrode material, interface resistance and ionic resistance of electrolyte. To quantitatively compare the values of R_{ct}, R_s, an equivalent circuit (lower inset in Figure 5e) was constructed for the fitting. The higher R_s (Table S3) of PMX1 and PMX2 than MX and CMX manifests that the phosphorus incorporation causes decreased electrical conductivity of MXene. This decrement in conductivity is also observed in PMX8 and PMX20 with higher phosphorus content (Figure S10c). The phosphorous doping induced lattice distortion and amorphization are regarded to be responsible for the decrement in conductivity. In addition, the changed surface functionalization also leads to the decrement of density of states at Femi level, [28] which is another reason for the decreased electrical conductivity in phosphorus-doped MXenes. It is also observed from Table S3 that phosphorus doping contributes to smaller R_{ct}, indicative of increased active sites in PMX1 and PMX2.

The redox reactions of $Ti_3C_2T_x$ MXene are governed by reversible proton bonding-debonding on surface -O terminations.[38, 39] The charge storage in the sample can be divided into diffusion-controlled and capacitive parts,

$$i(V) = k_1 v + k_2 v^{0.5} \qquad (1)$$

where the current density at fixed potential, $i(V)$, is regarded as the sum of capacitive ($k_1 v$) and diffusion controlled ($k_2 v^{0.5}$) components. The constants k_1 and k_2 can be obtained by linear fitting of the plots of $i(V)/v^{0.5}$ vs. $v^{0.5}$. The results show that the capacitive contribution rises with increasing scan rates in all samples, while PMX2 always exhibits a higher ratio of capacitive contribution than other samples at scan rates of 2 ~ 50 mV s^{-1} (Figure S11). Figure 5f compares the contributions to total capacitance of the four samples at 2 mV s^{-1}, where the diffusion-controlled capacitance of all the samples exhibits little difference. Clear distinctions are observed from capacitive contribution. PMX2 shows the highest capacitance (361 F g^{-1}) from capacitive process. Therefore, we conclude that phosphorus incorporation can boost capacitive performance of $Ti_3C_2T_x$ MXene. PMX2 was cycled at 10 A g^{-1} and 94.3 % capacitance was retained after 20000 cycles, suggesting its robust structure and good prospect for supercapacitor electrodes.

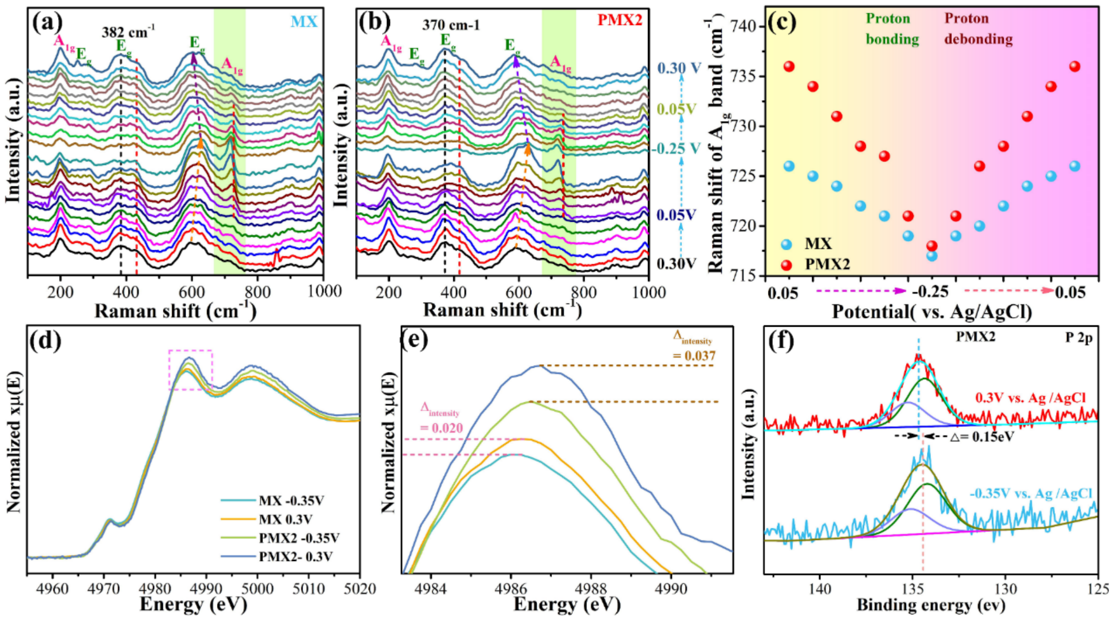

Figure 6 *In situ* Raman spectra of (a) MX and (b) PMX2 at potential range of -0.25 ~ 0.30 V versus Ag/AgCl reference electrode. (c) Raman shift of A_{1g} band of MX and PMX2 with applied potential. (d) Ti K-edge XANES spectra of MX and PMX2 at -0.35 and 0.30 V versus Ag/AgCl, and (e) enlarged profile of the rectangular area in (d). (f) P 2p XPS spectrum of PMX2 at -0.35 and 0.30 V versus Ag/AgCl.

Though the boosting effect of phosphorus on EC performance of $Ti_3C_2T_x$ MXene has been confirmed in the previous discussion, the underlying mechanism on the enhancement is still unclear. *Ex situ* XRD results (Figure S12) first reveal that MX, PMX2 and CMX show different interlayer distances at -0.35 and 0.30 V vs. Ag/AgCl, indicating their intercalation mechanism in pseudo-capacitive energy storage as reported in literature.[40] When the applied potential decreases from 0.30 to -0.35 V, all the samples show a decreased interlayer spacing since the intercalated protons increase the electrostatic attraction between MXene layers.[8, 40]

The redox reaction of $Ti_3C_2T_x$ MXene involves the change of titanium valence states,[16] which was investigated through in situ Raman,[41] ex situ XPS[42] and in situ XANES.[16] In situ Raman characterization was conducted in a homemade device (Figure S13). The Raman spectra of MX and PMX2 at potentials from -0.25 to 0.30 V vs. Ag/AgCl are shown in Figure 6a-b, measured using a homemade device (Figure S13). The E_g band at 230 ~ 470 cm^{-1} has not shown evident shift with the applied potentials, while both E_g (500 ~ 690 cm^{-1}) and A_{1g} (~720 cm^{-1}) bands exhibit a reversible peak shift with the applied potentials. The shift of these two bands in pristine MX is due to the bonding/debonding of protons with surface -O functional groups.[34] The similar change observed in PMX2 verifies its similar electrochemical behavior. Noting that the peak shift of the A_{1g} (~720 cm^{-1}) band is associated with the change of titanium valence states,[41] we compare the peak positions of the A_{1g} bands of the two samples at potentials from -0.25 to 0.30 V vs. Ag/AgCl in Figure 5c. The variation range of the peak position of A_{1g} band in PMX2 is 718~736 cm^{-1}, which is much broader than that of MX (717~726 cm^{-1}), indicative of greater change of titanium valence states occurring in PMX2. To further affirm the more pronounced variation of titanium valence state in PMX2, XANES and XPS spectra of MX and PMX2 at -0.35 and 0.30 V vs. Ag/AgCl were also collected and compared. The change of white-line peak intensity in Ti K-edge XANES can reflect its variation on valence state.[43] The white-line peak of the XANES spectrum of PMX2 exhibits a higher intensity difference than that of MX (0.037 vs. 0.020) between -0.35 and 0.30 V vs. Ag/AgCl potentials (Figure 6 d-e), validating the larger variation of titanium valence state in PMX2. Consistently, *ex situ* XPS results (Figure S14) also demonstrate the identical trend. S 2p XPS spectra of residual sulfate radicals (SO_4^{2-}) in all samples were used for calibration because of its nonparticipation in the redox action (Figure S15). The shift of right edge in normalized Ti 2p3 peaks was used to evaluate the change of titanium valence state (Figure S14). The edge shifts in MX and PMX2 are confirmed as 0.13 and 0.07 eV, respectively, indicating the more electron gain and loss in PMX2 during the charge/discharge process. In addition, the P 2p XPS spectra of PXM2 at -0.35 and 0.30 V vs. Ag/AgCl were also studied (Figure 6f). A 0.15 eV difference in binding energies of the two spectra elucidates that the surface grafted phosphorus atoms involve in the energy storage process. It has been reported that one oxygen termination on $Ti_3C_2T_x$ MXene bonds with one proton, contributing to pseudocapacitance.[17, 40, 44] While in the current case, as shown by DFT calculations (Figure S16), one surface grafted phosphorus can bond with two protons, more than pure oxygen termination does, resulting in more charge storage. In addition, differential charge density distributions results (Figure S17) further verify that this two-proton bonding process also induce charge transfer in titanium of $Ti_3C_2T_x$ MXene to protons.

Based on above results and discussion, it can be summarized that the surface grafted phosphorus serves as new active sites to enable two-proton bonding/debonding process, which can boost greater change of titanium valence sate in $Ti_3C_2T_x$ and lead to more charge transfer during its charge/discharge process, contributing to enhanced specific capacitance.

Finally, PMX2 was selected to assemble a symmetric supercapacitor to evaluate the practicability of phosphorus doped $Ti_3C_2T_x$ MXene. The resultant device exhibits a voltage window of 1 V and delivers a maximum capacitance of 97 F g^{-1} based on the total mass of two electrodes at 2 mV s^{-1}, superior to the device assembled with MX, as shown in Figure S18a-b. The PMX2-based supercapacitor delivers 85.6% of the initial capacitance after 10000 GCD cycles at 5 A g^{-1} (Figure S18c), justifying the remarkable stability of the PMX2 electrode. In addition, the Ragone plots (Figure S18d) show that the PMX2-based device exhibits a maximum energy density of 13.41 Wh Kg^{-1} at the power density of 97 W Kg^{-1} and retains 5.99 Wh Kg^{-1} at 4310 W Kg^{-1}, which not only excels those of MX-based devices, but also outperforms KOH treated (washing + annealing) $Ti_3C_2T_x$ MXene (7.25 Wh Kg^{-1} at 250 W Kg^{-1}),[42] porous $Ti_3C_2T_x$ MXene film (9.2 Wh Kg-1 at 100 W Kg^{-1}),[45] and N, S co-doped $Ti_3C_2T_x$ MXene (3.19 Wh Kg^{-1} at 349 W Kg^{-1}),[46] proving the competent role played by the grafted phosphorus on $Ti_3C_2T_x$ MXene in boosting its supercapacitive performance.

3. Conclusions

In summary, we demonstrate a phosphorus doping strategy that achieves the only formation of P-O doped species in $Ti_3C_2T_x$ MXene by grafting phosphorus atoms onto its surface through oxygen bridging. The underlying mechanism that how this type of species boosts capacitive performance of $Ti_3C_2T_x$ MXene is also revealed. The resultant PMX2 exhibits enhanced electrochemical performance than pristine MXene and delivers a maximum capacitance of 437 F g^{-1} at 2 mV s^{-1} in 1M H_2SO_4 aqueous electrolyte along with excellent stability (94.3% capacitance retention after 20000 cycles). The phosphorus atoms of P-O bonds on $Ti_3C_2T_x$ MXene serve as new active sites to enable a two-proton bonding-debonding process, contributing to improved charge transfer and energy storage ability in P-doped $Ti_3C_2T_x$ MXene. However, too much surface P-doping is detrimental due to the damage of crystal structure of MXene. It is believed that our work paves a way for doping MXene with other heteroatoms to achieve even better performance modulation.

Methods and experimental section

Preparation of $Ti_3C_2T_x$ MXene aerogel

$Ti_3C_2T_x$ MXene aerogel was prepared by a two-step method. $Ti_3C_2T_x$ colloidal solution was firstly synthesized by the minimal intensive layer delamination (MILD) method.[47] Two grams of 400 mesh Ti_3AlC_2 precursor was slowly added into 40 ml 9 M HCl +3.2 g LiF etchant, followed by water bath heating at 40 °C and continuously stirring under Ar bubbling for 24 h. The resultant product was washed via repetitive 3500 rpm × 5min centrifugation procedures until pH of the supernatant reaches to 6. After the supernatant was decanted, extra deionized (DI) water was poured into the centrifugation tube, which was then loaded onto an orbital shaker for delaminating MXene. Finally, black supernatant in the tube was collected after centrifuging at 3500 rpm for 60 min for next fabrication step. Note that shaking for one time is not enough to delaminate all multilayered MXene, so here multiple shaking and collections were conducted to increase the yield. In our experiment, around 600 ml 2.9 g ml^{-1} MXene solution was eventually obtained.

The $Ti_3C_2T_x$ MXene colloidal solution were frozen in liquid nitrogen for 10 min to assemble MXene aerogel framework, followed by vacuum drying at -65°C in a freeze-drying machine for five days (pressure $<1\times 10^{-3}$ atm) in the second step. The water between MXene sheets was vaporized during this procedure, generating final porous

MXene aerogel (Figure S1b).

Synthesis of phosphorus grafted $Ti_3C_2T_x$

Grafting phosphorus atoms onto $Ti_3C_2T_x$ was conducted in a tube furnace with two temperature regions. Certain amount of NaH_2PO_2 and 50 mg as-prepared $Ti_3C_2T_x$ aerogel were put at the upstream and downwind temperature regions and heated at 350 and 400 °C, respectively, under continuous 50 sccm argon flow. In details, the phosphine produced in the first region flows to downstream heated MXene to achieve surface phosphorus graft. The mass ratio between NaH_2PO_2 and MXene was controlled as 1, 2, 8 and 20, with the corresponding synthesized samples named as PMX1, PMX2, PMX8 and PMX20, respectively.

Materials characterization

The morphologies and microstructure of synthesized samples were characterized by Scanning Electron Microscope (SEM, JEOL Model JSM-6490) equipped with energy dispersive X-ray spectrometry (EDS) system and Scanning Transmission Electron Microscopy (STEM). X-ray diffraction (XRD) patterns of the samples were recorded using an X-ray Diffractometer (Rigaku SmartLab) with monochromatic Cu Kα X-ray source (λ=0.15406 nm). Specific area and pore size distribution of the samples were characterized through a MICROMERITICS surface area and porosity analyzer (ASAP2020). The chemical composition and elemental valence states of the samples were investigated on a Nexsa G2 XPS system equipped with monochromatic and focused 12 kV aluminum Kα X-Ray. Raman spectra including in situ Raman spectra were measured in a WITEC Confocal Raman system (Alpha300 R).

Electrochemical measurements

The slurry for working electrodes was made through mixing MXene sample, carbon black and PVDF with a mass ratio of 8:1:1 in 600 μL N-Methylpyrrolidone (NMP) with continuous grinding for 30 min. The resultant slurry was then coated on 2 × 3 cm^2 graphite paper, followed by vacuum drying at 80°C for 6h to obtain working electrodes (~2.2 mg cm^{-2} active material loading). Supercapacitive performance of working electrodes was investigated through a three-electrode configuration with Ag/AgCl (sat. KCl), graphite bar and 1M H_2SO_4 as reference electrode, counter electrode and electrolyte, respectively, conducted on a SOLARTRON electrochemical workstation. For assembling symmetric supercapacitors, two Φ14 mm working electrodes were separated by a Nafion 117 film and a glass fiber membrane, and then assembled in a Swagelok cell, followed by injecting 200μL 1M H_2SO_4 electrolyte. The energy storage ability of symmetric supercapacitors was also studied through the SOLARTRON workstation. The cyclic stability of both working electrodes and symmetric supercapacitors was all conducted on an Arbin Battery testing system.

Acknowledgements

This work was supported by the Hong Kong Polytechnic University (CD8W, and SAC1).

References

[1] M. Hu, H. Zhang, T. Hu, B. Fan, X. Wang and Z. Li, *Chem. Soc. Rev.* **2020**, 49, 6666.

[2] H. Liu, W. Lei, Z. Tong, X. Li, Z. Wu, Q. Jia, S. Zhang and H. Zhang, *Advanced Materials Interfaces* **2020**, 7.

[3] H. Cui, Y. Guo, W. Ma and Z. Zhou, *ChemSusChem* **2020**, 13, 1155.

[4] R. Wang, M. Li, K. Sun, Y. Zhang, J. Li and W. Bao, *Small* **2022**, 18, e2201740.

[5] Y. Deng, Y. Xie, K. Zou and X. Ji, *J. Mater. Chem. A* **2016**, 4, 1144.

[6] Z. Li, S. Gadipelli, Y. Yang, G. He, J. Guo, J. Li, Y. Lu, C. A. Howard, D. J. L. Brett, I. P. Parkin, F. Li and Z. Guo, *Energy Storage Materials* **2019**, 17, 12.

[7] M. Naguib, M. Kurtoglu, V. Presser, J. Lu, J. Niu, M. Heon, L. Hultman, Y. Gogotsi and M. W. Barsoum, *Adv. Mater.* **2011**, 23, 4248.

[8] M. R. Lukatskaya, O. Mashtalir, C. E. Ren, Y. Dall'Agnese, P. Rozier, P. L. Taberna, M. Naguib, P. Simon, M. W. Barsoum and Y. Gogotsi, *Science* **2013**, 341, 1502.

[9] M. Ghidiu, M. R. Lukatskaya, M. Q. Zhao, Y. Gogotsi and M. W. Barsoum, *Nature* **2014**, 516, 78.

[10] A. Shayesteh Zeraati, S. A. Mirkhani, P. Sun, M. Naguib, P. V. Braun and U. Sundararaj, *Nanoscale* **2021**, 13, 3572.

[11] C. Lu, L. Yang, B. Yan, L. Sun, P. Zhang, W. Zhang and Z. Sun, *Adv. Funct. Mater.* **2020**, 30, 2000852.

[12] Y. Wei, P. Zhang, R. A. Soomro, Q. Zhu and B. Xu, *Adv. Mater.* **2021**, 33, 2103148.

[13] C. Liu, Y. Bai, W. Li, F. Yang, G. Zhang and H. Pang, *Angew. Chem. Int. Ed. Engl.* **2022**, 61, e202116282.

[14] M. Alhabeb, K. Maleski, B. Anasori, P. Lelyukh, L. Clark, S. Sin and Y. Gogotsi, *Chem. Mater.* **2017**, 29, 7633.

[15] M. Benchakar, L. Loupias, C. Garnero, T. Bilyk, C. Morais, C. Canaff, N. Guignard, S. Morisset, H. Pazniak, S. Hurand, P. Chartier, J. Pacaud, V. Mauchamp, M. W. Barsoum, A. Habrioux and S. Célérier, *Appl. Surf. Sci.* **2020**, 530.

[16] M. R. Lukatskaya, S.-M. Bak, X. Yu, X.-Q. Yang, M. W. Barsoum and Y. Gogotsi, *Adv. Energy Mater.* **2015**, 5.

[17] H. Shao, K. Xu, Y.-C. Wu, A. Iadecola, L. Liu, H. Ma, L. Qu, E. Raymundo-Piñero, J. Zhu, Z. Lin, P.-L. Taberna and P. Simon, *ACS Energy Lett.* **2020**, 5, 2873.

[18] Y. Wen, R. Li, J. Liu, Z. Wei, S. Li, L. Du, K. Zu, Z. Li, Y. Pan and H. Hu, *J. Colloid Interface Sci.* **2021**, 604, 239.

[19] X. Wei, M. Cai, F. Yuan, D. Lu, C. Li, H. Huang, S. Xu, X. Liang, W. Zhou and J. Guo, *Appl. Surf. Sci.* **2022**, 606.

[20] N. Gupta, R. K. Sahu, T. Mishra and P. Bhattacharya, *J. Mater. Chem. A* **2022**, 10, 15794.

[21] L. Chen, Y. Bi, Y. Jing, J. Dai, Z. Li, C. Sun, A. Meng, H. Xie and M. Hu, *Molecules* **2023**, 28.

[22] W. Bao, X. Tang, X. Guo, S. Choi, C. Wang, Y. Gogotsi and G. Wang, *Joule* **2018**, 2, 778.

[23] M. Hu, R. Cheng, Z. Li, T. Hu, H. Zhang, C. Shi, J. Yang, C. Cui, C. Zhang, H. Wang, B. Fan, X. Wang and Q. H. Yang, *Nanoscale* **2020**, 12, 763.

[24] H. Li, H. Zhou, L. Zhuang, T. Liu, W. Han and H. Huang, *Advanced Energy and Sustainability Research* **2022**, 3, 2100216.

[25] W. Liu, Y. Zheng, Z. Zhang, Y. Zhang, Y. Wu, H. Gao, J. Su and Y. Gao, *J. Power Sources* **2022**, 521.

[26] M. Naguib, O. Mashtalir, J. Carle, V. Presser, J. Lu, L. Hultman, Y. Gogotsi and M. W. Barsoum, *ACS Nano* **2012**, 6, 1332.

[27] H. Pazniak, M. Benchakar, T. Bilyk, A. Liedl, Y. Busby, C. Noel, P. Chartier, S. Hurand, M. Marteau, L. Houssiau, R. Larciprete, P. Lacovig, D. Lizzit, E. Tosi, S. Lizzit, J. Pacaud, S. Celerier, V. Mauchamp and M. L. David, *ACS Nano* **2021**, 15, 4245.

[28] J. L. Hart, K. Hantanasirisakul, A. C. Lang, B. Anasori, D. Pinto, Y. Pivak, J. T. van Omme, S. J. May, Y. Gogotsi and M. L. Taheri, *Nat Commun* **2019**, 10, 522.

[29] V. Natu, M. Benchakar, C. Canaff, A. Habrioux, S. Célérier and M. W. Barsoum, *Matter* **2021**, 4, 1224.

[30] F. Zhou, X.-S. Yang, J. Liu, J. Liu, R. Hu, L. Ouyang and M. Zhu, *J. Power Sources* **2021**, 485.

[31] J. Halim, K. M. Cook, M. Naguib, P. Eklund, Y. Gogotsi, J. Rosen and M. W. Barsoum, *Appl. Surf. Sci.* **2016**, 362, 406.

[32] R. Meng, J. Huang, Y. Feng, L. Zu, C. Peng, L. Zheng, L. Zheng, Z. Chen, G. Liu, B. Chen, Y. Mi and J. Yang, *Adv. Energy Mater.* **2018**, 8.

[33] X. Chen, Y. Zhu, M. Zhang, J. Sui, W. Peng, Y. Li, G. Zhang, F. Zhang and X. Fan, *ACS Nano* **2019**, 13, 9449.

[34] A. Sarycheva and Y. Gogotsi, *Chem. Mater.* **2020**, 32, 3480.

[35] N. Zhao, Y. Yang, D. Yi, Y. Xiao, K. Wang, W. Cui and X. Wang, *Chem. Eng. J.* **2021**, 422.

[36] Y. Wen, T. E. Rufford, X. Chen, N. Li, M. Lyu, L. Dai and L. Wang, *Nano Energy* **2017**, 38, 368.

[37] K. Tao, Y. Gong and J. Lin, *Nano Energy* **2019**, 55, 65.

[38] M. R. Lukatskaya, S. Kota, Z. Lin, M.-Q. Zhao, N. Shpigel, M. D. Levi, J. Halim, P.-L. Taberna, M. W. Barsoum, P. Simon and Y. Gogotsi, *Nat. Energy* **2017**, 2, 17105.

[39] S. Fleischmann, Y. Zhang, X. Wang, P. T. Cummings, J. Wu, P. Simon, Y. Gogotsi, V. Presser and V. Augustyn, *Nat. Energy* **2022**, 7, 222.

[40] X. Mu, D. Wang, F. Du, G. Chen, C. Wang, Y. Wei, Y. Gogotsi, Y. Gao and Y. Dall'Agnese, *Adv. Funct. Mater.* **2019**, 29, 1902953.

[41] P. Salles, D. Pinto, K. Hantanasirisakul, K. Maleski, C. E. Shuck and Y. Gogotsi, *Adv. Funct. Mater.* **2019**, 29.

[42] J. Li, X. Yuan, C. Lin, Y. Yang, L. Xu, X. Du, J. Xie, J. Lin and J. Sun, *Adv. Energy Mater.* **2017**, 7.

[43] Y. Tang, Y. Zhang, O. I. Malyi, N. Bucher, H. Xia, S. Xi, Z. Zhu, Z. Lv, W. Li, J. Wei, M. Srinivasan, A. Borgna, M. Antonietti, Y. Du and X. Chen, *Adv. Mater.* **2018**, 30, 1802200.

[44] Y. Sun, C. Zhan, P. R. C. Kent, M. Naguib, Y. Gogotsi and D. E. Jiang, *ACS Appl. Mater. Interfaces* **2020**, 12, 763.

[45] P. Zhang, Q. Zhu, R. A. Soomro, S. He, N. Sun, N. Qiao and B. Xu, *Adv. Funct. Mater.* **2020**, 30.

[46] L. Liao, D. Jiang, K. Zheng, M. Zhang and J. Liu, *Adv. Funct. Mater.* **2021**, 31, 2103960.

[47] J. Zhang, N. Kong, S. Uzun, A. Levitt, S. Seyedin, P. A. Lynch, S. Qin, M. Han, W. Yang, J. Liu, X. Wang, Y. Gogotsi and J. M. Razal, *Adv. Mater.* **2020**, 32, 2001093.